2015-1495

A Damage Assessment for Wind Turbine Blades from Heavy Atmospheric Particles

Giovanni Fiore,* Gustavo E. C. Fujiwara,† and Michael S. Selig‡
University of Illinois at Urbana-Champaign, Department of Aerospace Engineering, Urbana, IL 61801

A numerical study of how to simulate heavy atmospheric particle collisions with a 38-m, 1.5-MW horizontal axis wind turbine blade is discussed. Two types of particles were considered, namely hailstones and rain drops. Computations were performed by using a two-dimensional inviscid flowfield solver along with a particle position predictor code. Three blade sections were considered: at 35% span and characterized by a DU 97-W-300 airfoil, at 70% span with a DU 96-W-212 airfoil, and at 90% span using a DU 96-W-180 airfoil. The three blade sections are constituted by 8-ply carbon/epoxy panels, coated with ultra-high molecular weight polyethylene (UHMWPE). Hailstone and raindrop simulations were performed to estimate the location of the striking occurrences and the blade surface area subject to damage. Results show that the impact locations along the blade are a function of airfoil angle of attack, local relative velocity, airfoil shape, aerodynamics and mass of the particle. Hailstones were found to collide on nearly every portion of the blade section along their trajectory due to their insensitivity to the blade flowfield. The damaged surface areas were found to be small when compared to the overall impingement surface, and most of delamination damage was localized on the blade leading edge. Moreover, panel delamination occurred for outboard sections, when $r/R \geq 0.90$. The damage due to raindrops was divided in an erosive and a fatigue contribution due to the impact force. It was observed that the erosive damage follows the cubic power of the blade velocity, whereas the impact force follows the square power of the blade velocity. Moreover, it was seen that the rain drops are sensitive to the blade flowfield, due to shape modifications through the Weber number. In particular, a sensitive behavior of the damage with respect to the blade angle of attack was observed.

Nomenclature

a	=	axial induction factor
A	=	particle reference area
AK	=	particle nondimensional mass
b_C	=	coating constant related to the fatigue curve
c	=	airfoil chord length
C	=	speed of sound
COE	=	Cost of Energy
C_d	=	airfoil drag coefficient
C_D	=	particle drag coefficient
C_l	=	airfoil lift coefficient
d	=	particle diameter
D	=	particle drag force
E	=	erosion rate
E_D	=	particle damage efficiency

*Graduate Student (Ph.D.), Department of Aerospace Engineering, 104 S. Wright St., AIAA Student Member.
†Graduate Student (Ph.D.), Department of Aerospace Engineering, 104 S. Wright St., AIAA Student Member.
‡Associate Professor, Department of Aerospace Engineering, 104 S. Wright St., AIAA Associate Fellow.
http://www.ae.illinois.edu/m-selig

E_I = particle impact efficiency
F_{imp} = particle impact force
FTE = failure threshold energy
FTV = failure threshold velocity
g = gravitational acceleration
$GAEP$ = Gross Annual Energy Production
h = airfoil projected height perpendicular to freestream
$\overline{k}$ = number of coating stress wave reflections
m = particle mass
n_i = number of droplet impacts per site during incubation period
P = impact pressure
r/R = blade section radial location
R_D = damage surface ratio
R_I = impingement surface ratio
Re = particle Reynolds number
Re_∞ = freestream Reynolds number
s = impact location in airfoil arc lengths
$S_{eff,C}$ = effective coating strength
s_{tot} = airfoil total arc length
t = time
t/c = airfoil thickness-to-chord ratio
U = chordwise flowfield velocity component
V = chord-normal flowfield velocity component
V_{dam} = hailstone damage velocity
V_{imp} = particle impact velocity
V_N = particle normal impact velocity
V_r = blade relative wind velocity
V_{rel} = particle relative drop velocity
V_s = particle slip velocity
V_{term} = particle terminal velocity
We = droplet Weber number
x = particle x-location
y = particle y-location
Z = impedance
α = angle of attack
α_r = relative angle between flowfield and particle velocity
β = impingement efficiency
γ = parameter related to coating thickness
δ = thickness
η_D = particle damage ratio
λ = tip-speed ratio
θ = impact angle
μ = dynamic viscosity
ν = Poisson's ratio
ρ = density
σ = surface tension
$\overline{\sigma_C}$ = coating average surface stress
$\sigma_{u,C}$ = coating ultimate tensile strength
τ = nondimensional time
ψ = impedance ratio

Subscripts and superscripts

0	=	initial state
C	=	coating
H	=	hail
l	=	lower limit
P	=	particle
R	=	rain
S	=	substrate
u	=	upper limit

I. Introduction

Wind turbines used for eletrical power generation are subject to fouling and damage by airborne particles typical of the environment where the wind turbine operates. Throughout the 20-year lifespan of a wind turbine, particles such as rain, sand, ice crystals, hail, and insects are major contributors to a deterioration in turbine performances through local airfoil surface alterations.[1–6] Wind turbine blades accumulate dirt especially in the surroundings of the leading edge. Moreover particle collision, temperature jumps and freeze-thaw cycles may cause smaller coating cracks to propagate, promoting coating removal and eventually delamination and corrosion damage due to exposure of the internal composite structure. The originally smooth surface of the blades may change considerably, and the increased roughness will cause a drop of gross annual energy production (GAEP) and an increase in cost of energy (COE)[7–13].

The weather conditions of a given wind farm site may vary substantially throughout the seasons. For geographical locations subject to frequent precipitations, the repetitive impact with raindrops may increase the mechanical fatigue in the blade surface materials[14,15] and large droplets may cause potential panel delamination.[16,17] A more severe situation is represented by hailstorms. High potential wind resource sites such as those found in the Great Plains of the United States (north western Texas, eastern Colorado, north eastern Oklahoma, and southern Kansas),[18] are characterized by larger hailstorm risk factors than any other location in the US territory.[19] Anticyclonic supercells typical of the Colorado Plains have been recorded to easily produce hailstones greater than 50 mm (1.97 in) in diameter.[20] Soon after the installation of large wind farms over the western Great Plains in early 2000, wind turbines were reported to be damaged by heavy hailstorms.[21] Hailstones are larger, heavier and harder than raindrops, and may strike in the vicinity of the leading edge at relative velocities and impact energies capable of not only internal delamination, but also permanent indentation, cracking and eventually penetration of the composite panel.[6,22,23]

Wind farm operators are forced to schedule blade inspection and maintenance to reduce the cost of ineffective electric power production due to degraded blade surfaces. Disassembling a wind turbine for factory inspection is costly, so the majority of servicing is performed on site. Damaged areas are located through visual inspection of the blade, surface alterations are smoothed through primer application and a protective polyurethane-based film is applied.[11,24] However, because of the highly competitive nature of the wind turbine industry, the majority of wind turbine manufacturers are reluctant to share details of the construction materials with maintenance companies. Therefore, technical expertise has a tremendous weight on blade repair success and effectiveness.[4,22] Moreover, repairs are mostly performed in the vicinity of the leading edge and not necessarily on all areas exposed to damage. Farther downstream, blade areas that do not manifest large damages may be left untreated, promoting the enlargement of surface imperfections starting where the coating is weaker. An estimated 6% of the overall repairs and maintenance resources for wind turbines is dedicated to rotor blades.[6,25] Moreover, an analysis of wind turbine reliability showed that tip break and blade damage are the first and third most common failure modes for wind turbines, respectively.[6]

To complicate the blade maintenance scenario, the damage due to heavy particles is challenging to detect. An emerging issue for damage assessment is posed by damage that is not visually evident. Barely visible impact damage has large potential for not being detected during servicing.[4,6,26] Spar caps that were damaged by severe hailstorms may appear intact at a first look, but may have reduced maximum structural loads.[27] Advanced nondestructive inspection tools (NDI), such as ultrasound scan and shearography of the composite sandwich are currently increasing in popularity but still represent a smaller fraction of actual servicing applications.[26] Major technological challenges of NDI tools are represented by poorly accessible conditions and large surface areas typical of wind turbines blades.[6]

Since modern wind turbine designers make large use of composite materials,[21,28] the investigation of the hailstone damage problem follows an identical approach to assessing damage to modern composite aircraft and ship structures.[17,22,26] Driven by such considerations, experimental and numerical studies of hailstone impact were performed to simulate the damage tolerance of various aerospace-related composite materials.[23,27,29] A variety of collision angles and impact speeds were simulated, and such conditions are also typical for the hail-wind turbine scenario. These studies show that the severity of panel damage is a function of hailstone kinetic impact energy and impact angle, along with the structural characteristics of the composite panel.

The goal of this study was to numerically describe the trajectory of hailstones and rain drops and to characterize the impact areas of three sections along a wind turbine blade, located at 35%, 70% and 90% of the span. Damage models are implemented to characterize the blade for hailstone and droplet damage. A 3-blade, 38-m radius, 1.5-MW HAWT has been chosen to be representative of existing wind turbine systems, being the most common configuration in North America at present.[18] This paper is divided into five sections: the numerical method used is explained in Section II, the blade operating point, particle aerodynamics and damage models are introduced in Sec. III, while the results obtained are discussed in Sec. IV. Finally, conclusions are proposed in Sec. V.

II. Methodology and Theoretical Development

Predicting the trajectory of impinging particles is critical when impact characteristics on the wind turbine blade need to be determined. A lagrangian formulation code was developed in-house and named BugFoil.[30] BugFoil integrates a pre-existing insect trajectory code[31] and a customized version of XFOIL.[32] Local flowfield velocity components are obtained by querying the potential flow routine built in XFOIL, from which the particle trajectory and impact location on the airfoil are computed. Similarly, the capabilities of BugFoil have been expanded to simulate trajectories of hailstones and raindrops as well.

In steady flight, the forces acting on the particle are perfectly balanced and perturbations to such forces are assumed to be additive to the steady-state forces. For these reasons the equations of motion may be expressed by neglecting the steady-state forces and may be written as functions of increments only.[33] In the current study, both raindrops and hailstones were treated as aerodynamic bodies whose only associated force is the aerodynamic drag D.

By applying Newton's second law along the particle trajectory in both chordwise x and chord-normal y directions, the following equations are obtained[30,34–37]

$$m_P \frac{d^2 x_P}{dt^2} = \Sigma F_x \tag{1}$$

$$m_P \frac{d^2 y_P}{dt^2} = \Sigma F_y \tag{2}$$

By projecting the drag of the particle D in both chordwise x and chord-normal y directions using the relative angle between particle and flowfield velocity α_r, the equations may be rewritten as

$$m_P \frac{d^2 x_P}{dt^2} = \Delta D \cos\alpha_r \tag{3}$$

$$m_P \frac{d^2 y_P}{dt^2} = \Delta D \sin\alpha_r \tag{4}$$

Given the particle velocity components U_P and V_P and given the velocity flowfield components U and V at a certain point along the trajectory, the particle slip velocity V_s can be expressed as

$$V_s = \sqrt{(U-U_P)^2 + (V-V_P)^2} \tag{5}$$

while the trigonometric functions in Eqs. (3) and (4) may assume the form

$$\cos\alpha_r = \frac{U-U_P}{V_s} = \frac{V_{rx}}{V_s} \tag{6}$$

$$\sin\alpha_r = \frac{V-V_P}{V_s} = \frac{V_{ry}}{V_s} \tag{7}$$

By expressing the particle aerodynamic drag D as a function of dynamic pressure and by substituting for the trigonometric functions, the Eqs. (3) and (4) may be rewritten as

$$m_P \frac{d^2 x_P}{dt^2} = \frac{1}{2}\,\rho\, V_s^2\, A_P\, C_D\, \frac{V_{rx}}{V_s} \tag{8}$$

$$m_P \frac{d^2 y_P}{dt^2} = \frac{1}{2}\,\rho\, V_s^2\, A_P\, C_D\, \frac{V_{ry}}{V_s} \tag{9}$$

To scale this problem in a non-dimensional fashion, non-dimensional time, space, and mass parameters can be introduced here

$$\tau = \frac{t\,U}{c} \tag{10}$$

$$\bar{x}_P = \frac{x_P}{c} \tag{11}$$

$$\bar{y}_P = \frac{y_P}{c} \tag{12}$$

$$AK = \frac{2\,m_P}{\rho\, A_P\, c} \tag{13}$$

Nondimensionalization of Eqs. (8) and (9) by a reference velocity U yield

$$\frac{d^2 \bar{x}_P}{d\tau^2} = \frac{1}{AK}\,\overline{V}_r\, C_D\, \overline{V}_{rx} \tag{14}$$

$$\frac{d^2 \bar{y}_P}{d\tau^2} = \frac{1}{AK}\,\overline{V}_r\, C_D\, \overline{V}_{ry} \tag{15}$$

which represents a set of second-order, nonlinear differential equations. Once the particle drag coefficient is evaluated, the trajectory can be computed by numerically solving both x and y equations.

III. Blade Damage Analysis

The selected wind turbine layout is a a 1.5-MW, 3-blade, 38-m radius, tip-speed ratio $\lambda = 8.7$ HAWT. Starting at the root of the blade and moving toward the tip, the airfoils utilized are the DU 97-W-300, -212, and -180 respectively. The thickness of the blade sections (t/c) and chord length (c) decrease along the span of the blade, in accordance to conventional wind turbine designs. A nominal wind speed of 10.5 m/s at the hub was proposed for quiet weather conditions. However, due to the wind conditions during a rainstorm or hailstorm, the actual considered wind speed was 18.4 m/s. Such wind speed augmentation was computed through an empirical formula, as explained in Ref.[38]. Finally, an axial induction factor of $a = 1/3$ was used for the relative inflow conditions. The blade properties and airfoil operating conditions are summarized in Table 1.

During the unperturbed drop, hailstones and rain drops reach terminal velocity V_{term} aligned with the gravitational force. However, the total particle velocity will form an angle with the blade rotational plane. In fact the resultant particle velocity $V_{tot,particle}$ will be the vector summation of V_{wind} and V_{term}, as shown in Fig. 1. Depending on the nature of the particle, V_{term} may vary and may drive the particle to hit at steeper or shallower angles onto the blade surface.

The materials used for estimating the blade damage are divided into two categories: blade coating and blade composite structure. The blade coating was chosen to be ultra-high molecular weight polyethylene (UHMWPE). Such choice was driven by a coherent approach with previous sand erosion studies.[30] The material used for the composite structure is carbon-epoxy T800/3900-2. Great interest is shown in the scientific literature for the hailstone damage assessment of such composite materials.[23,27,29,39,40]

Since modern wind turbines are operated close to their maximum lift-to-drag ratios,[3,41,42] the three blade sections were analyzed with XFOIL and three values of C_l were determined in the proximity of $(C_l/C_d)_{max}$. The operating conditions for the three blade sections are reported in Table 2. Simulations for impingement and damage due to hailstones and droplets were performed at three angles of attack corresponding to the C_l-values determined.

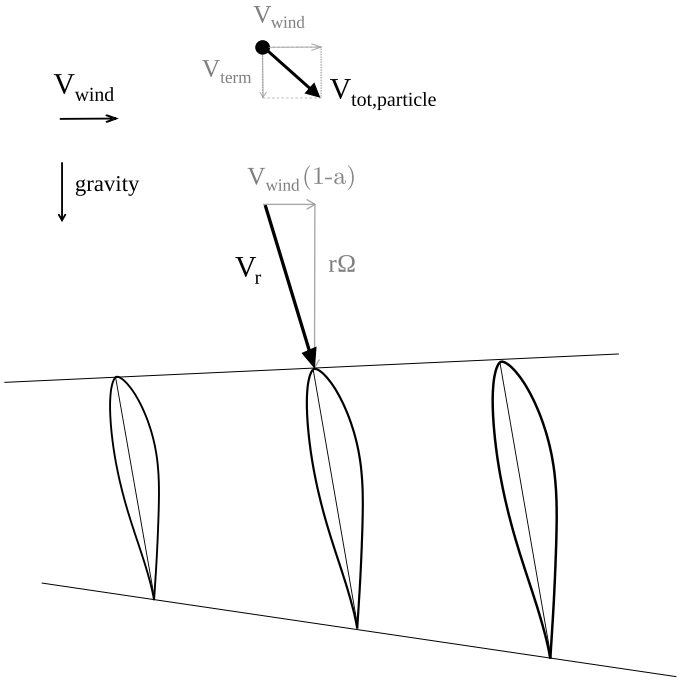

Figure 1. Particle and blade velocities: a – axial induction factor, Ω – angular velocity, r – local span V_r – blade relative wind.

Table 1. Baseline blade parameters

Location	r/R	Airfoil	c (m)	V_r (m/s)	Re
1	0.35	DU 97-W-300	3.13	34.30	7.39×10^6
2	0.70	DU 96-W-212	1.90	65.23	8.54×10^6
3	0.90	DU 96-W-180	1.20	83.28	6.88×10^6

A. Trajectory Evaluation

BugFoil is initialized using nondimensional input data. An equally-spaced array of particles is placed five chord-lengths upstream of the blade section, with inital velocity components nondimensionalized with respect to the local freestream velocity V_∞. Each particle is evaluated individually throughout its trajectory by numerically solving the particle equations of motion through a predictor-corrector algorithm. As the particle approaches the airfoil, the code verifies whether impingment occurs, and the impact locations over the airfoil are determined. By taking the derivative of the initial particle coordinate y^0 with respect to the particle impingement location in airfoil arc lengths s, the impingement efficiency is defined in the following manner[34]

$$\beta = \frac{dy^0}{ds} \tag{16}$$

The parameter β is an index of probability for the particle to impact with the airfoil. By computing trajectories for a vertical array of particles, the two outermost impacting trajectories correspond to $\beta = 0$. Those trajectories represent the upper and lower limits of impingement. The fraction of striking particles out of the total number is evaluated by localizing the initial upper and lower y-limits on the upstream array of particles, namely $y_I^{0,u}$ and $y_I^{0,l}$, as shown in Fig. 2. By dividing the distance between these two locations by the projected height of the airfoil h, the nondimensional impact efficiency parameter E_I is introduced as

$$E_I = \frac{y_I^{0,u} - y_I^{0,l}}{h} = \frac{\Delta y_I^0}{h} \tag{17}$$

The parameter E_I represents the height of the particle array captured by the airfoil, relative to the airfoil projected height. When simulating the trajectory of hailstones and droplets the local developed impact energy may cause damage

Table 2. Blade sections operating conditions

r/R	α (deg)	C_l	C_l/C_d
0.35	3.5	0.83	101.81
	5.5	1.09	126.52
	7.5	1.34	142.32
0.70	4.0	0.81	151.80
	6.0	1.04	151.24
	8.0	1.24	119.83
0.90	4.0	0.79	162.35
	6.0	1.02	175.21
	8.0	1.21	123.60

in the panel depending on the panel strength characteristics. To assess damage in the panel, the particle impact velocity can be compared to the failure threshold velocity FTV of the panel. A definition of damage efficiency E_D for hailstones can be used to compute the fraction of damaging particles out of the total impinging number

$$E_D = \frac{y_D^{0,u} - y_D^{0,l}}{h} = \frac{\Delta y_D^0}{h} \tag{18}$$

The relative quantity of damaging particles is given by the parameter damage ratio η_D defined as follows

$$\eta_D = \frac{E_D}{E_I} \tag{19}$$

The parameter η_D represents a figure of merit of the airfoil since it incorporates the damage mechanism of hailstones. An advantage of using η_D is the independency on airfoil projected height h, which may not have a linear relationship with the angle of attack of the airfoil.

One way to estimate the extent of blade surface subject to particle collisions is to compute the airfoil arc length within the upper and lower surface impingement limits, s_I^u and s_I^l, respectively, shown in Fig. 2. The result of this operation is called Δs_I. By knowing the airfoil total arc length s_{tot}, the impingement surface ratio R_I can be computed as

$$R_I = \frac{s_I^u - s_I^l}{s_{tot}} = \frac{\Delta s_I}{s_{tot}} \tag{20}$$

As R_I approaches the unity, a larger portion of the blade area is subject to particle collision. In a similar manner, when considering the panel damage, the damage surface ratio R_D may be defined as

$$R_D = \frac{s_D^u - s_D^l}{s_{tot}} = \frac{\Delta s_D}{s_{tot}} \tag{21}$$

The parameter R_D represents a direct measurement of the blade surface subject to damage.

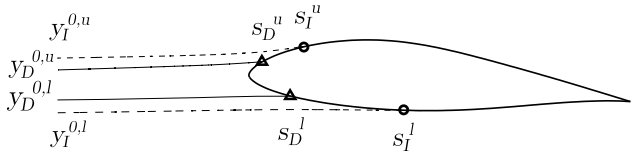

Figure 2. Definition of impact and damage limits.

B. Hailstone Background

1. Aerodynamics of the Hailstone

Hailstones are significantly larger and heavier than other airborne particles such as sand grains and insects. Hence, their aerodynamic behavior is significantly different from the behavior of other particles considered in previous studies.[30,43] The hailstone impacting trajectories largely deviate from the aerodynamic streamlines around the blade and impact occurs on a range of steep impact angles.

Choosing the representative hailstone characteristics for aerodynamic drag computation is somewhat subjective. In fact, hailstone dimensions and weight may vary significantly in different storms and geographic regions.[19] From a conservative standpoint, however, one can choose large and heavy hailstones as a reference. The chosen values of diameter and weight are 50.8 mm (2 in) and 61.8 g (2.18 oz), respectively, in accordance with U.S. weather reports,[20] along with experimental and numerical impact investigations.[23,29,39] Also, these hailstone characteristics are in good agreement with modern wind turbine design and maintenance recommendations outlined in Ref.[44].

During the unperturbed drop, hailstones reach terminal velocity V_{term} as a function of the aerodynamic drag coefficient $\overline{C_{D,H}}$, ice density ρ_H and stone diameter d_H. If the aerodynamic drag is equated to the gravitational force acting on the particle, the following expression of $V_{term,H}$ is obtained

$$V_{term,H} = \sqrt{\frac{4\ g\ d_H\ \rho_H}{3\ \overline{C_{D,H}}\ \rho}} \tag{22}$$

The underlying assumption is that the drag does not vary throughout the unperturbed drop. Hence, a typical value of $\overline{C_{D,H}} = 0.83$ is assumed until the trajectory is influenced by the wind turbine flowfield. Assuming the particle to be horizontally transported by the wind, the hailstone relative velocity V_{rel} will be the vector summation of $V_{term,H}$ and wind speed.

When the hailstone finally encounters the aerodynamic flowfield generated by the wind turbine, the aerodynamic forces acting on the particle change according to the particle relative flow, and hence relative Reynolds number. An equation for the sphere drag coefficient in the Reynolds number range typical of falling hailstones is given by[45]

$$C_{D,H} = \frac{24}{Re} + \frac{6}{1+Re^{1/2}} + 0.4 \tag{23}$$

Note that in order to use such a formula, it is first computed the relative flow seen by the hailstone and hence the relative Reynolds number. Also, because Eq. 23 is valid for $Re \leq 2.5 \times 10^5$, the hailstone drag coefficient is set to 0.1 past that range.[45,46] The lift coefficient of the hailstone is assumed to be negligible for this study.

As opposed to insects and sand grains,[30] hailstone approach the blade with a velocity that is the combination of $V_{term,H}$ and V_{wind}. It is assumed here that an increase in wind intensity is observed during the hailstorm. A way to estimate such an increase is by correcting the incoming wind speed ($V_{wind} =$ 10.5 m/s (23.5 mph)) with appropriate gust factors.[38] The relation to correct for V_{wind} is the following

$$\Delta V_{wind} = (F_g\ F_s - 1)\, V_{wind} \tag{24}$$

where F_g and F_s are the empirical mean gust factor and the empirical statistical factor, respectively. By selecting a gust duration of 10 s for a standard deviation above mean wind speed equal to 1, the resulting values are $F_g = 1.195$ and $F_s = 1.465$.

C. Hailstone Damage

The prediction of damage due to hailstones is derived from the definition of failure threshold velocity (FTV),[23,29] defined as the lowest velocity at which a composite panel is subject to delamination upon impact. Using this velocity, a failure threshold energy (FTE) can be defined as the kinetic energy of the damaging hailstone at impact

$$FTE = \frac{1}{2}\, m_H\, FTV^2 \tag{25}$$

By measuring the failure threshold velocity at normal impact FTE_{90}, the following trigonometric relationship holds

$$FTE\,(\theta) = \frac{FTE_{90}}{\sin\theta} = \frac{\frac{1}{2}\, m_H\, FTV_{90}^2}{\sin\theta} \tag{26}$$

Table 3. Hailstone computational parameters

r/R	Re	AK_H	d_H/c	$V^0_{x,H}/V_r$	$V^0_{y,H}/VV_r$	FTV_{90}/V_r
0.35	207740	15.9	1.62×10^{-2}	1.73	-0.088	2.65
0.70	316150	26.2	2.67×10^{-2}	1.39	0.022	1.39
0.90	379000	41.4	4.23×10^{-2}	1.30	0.029	1.09

where θ is the hailstone impact angle. Since mass of hailstone m_H is known, FTV_{90} can be determined and the nondimensional damage velocity can be estimated dividing by the relative drop velocity V_{rel}. Finally, the computed velocity at impact V_{imp} can be compared to the corresponding FTV of the panel for a given impact angle, and the blade section may be flagged with hailstone damage when an excessive velocity V_{dam} is reached, i.e.

$$V_{dam} = V_{imp} - FTV > 0 \tag{27}$$

This evaluative damage criteria allows for quick analysis of wind turbine configurations during the design phase, or for a posterior damage assessment for existing installations. In general, drivers of FTV are the structural characteristics of the composite material and impact angle of the particle. The materials used for this study are 8-ply, 1.59 mm (0.062 in) thick carbon/epoxy panels.[27,39]

Note that Eq. 22 gives an absolute terminal velocity of the hailstone. However, when considering the rotative motion of turbine blades, the relative velocity V_{rel} is the vector summation of the local blade translational velocity and hailstone terminal velocity. From a damage evaluation standpoint, the most restrictive case is represented by the blade travelling upward, with the leading edge perpendicular to the hailstone trajectory. In this situation the highest velocities and thus impact energies are developed.

An additional way to characterize the damage due to hailstones is by computing the peak impact force F_{imp} on the blade surface. A proposed form to estimate F_{imp} is given by the formula[17]

$$F_{imp} = m_H \ \frac{(V_{imp} \ \sin\theta)^2}{d_H} \tag{28}$$

Such formula was used in the literature to estimate the force due to water droplets[47,48] and it is here extended to hailstones for simplicity. The advantage of using Eq. 28 lies in the ease of implementation. In fact, implementing a more accurate formula would require a deep ballistic characterization of the target material. Despite these observations, results show that applying such formula brings to reasonable estimates of F_{imp}, when compared with instantaneous measurements from experimental setups.[23]

The computational parameters and initial conditions for hailstones are summarized in Table 3, where the relative hailstone drop velocity V_{rel} and failure threshold velocity FTV_{90} are nondimensionalized with respect to the blade relative wind V_r.

D. Raindrop Background

1. Aerodynamics of the Raindrop

In order to establish the initial conditions for the droplet simulations, the motion of a water droplet in its unperturbed descent needs to be evaluated. As opposed to the hailstone, the terminal velocity of a droplet follows the empirical law as[49–51]

$$V_{term,R} = 943 \ \left[1 - e^{-(d_R/1.77)^{1.47}}\right] \tag{29}$$

Again, the relative droplet velocity V_{rel} will be the vector summation of $V_{term,R}$ and the wind speed.

When approaching the wind turbine blade section, a water droplet is subject to a progressive shape modification due to the magnitude of aerodynamic forces with respect to the surface tension forces.[17,52–54] In fact, the relative flow seen by the droplet may cause deformation and even fragmentation before impact. The physical parameter that represents the ratio of aerodynamic forces with respect to the droplet surface tension is the Weber number (We), that is

$$We = \frac{\rho \ V^2_{rel} \ d_R}{\sigma_R} \tag{30}$$

Table 4. Material constants

Phase	Material	ρ (kg/m^3)	C (m/s)
Raindrop (R)	Water	1000	1464
Coating (C)	UHMWPE	930	861
Substrate (SS)	T800/3900-2	1590	2375

Because of the droplet shape modification throughout the flowfield, the particle drag coefficient needs to be estimated accordingly. In particular, it was observed that a steep increase in C_D just prior to impact occurred, and values of drag coefficient greater than of a circular disk appeared.[55] A quasi-steady model to describe the drag coefficient is proposed. The particle drag coefficient is computed as an additive correction $\Delta C_{D,R}$ to the spherical drag, as a function of We, that is[56]

$$\Delta C_{D,R} = We\left(0.2319 - 0.1579\ \log Re + 0.047\ (\log Re)^2 - 0.0042\ (\log Re)^3\right) \tag{31}$$

Such a formula is an empirical correction that allows for simple drag computation, greatly simplifying the mathematical approach. The considered raindrop diameter for the simulations is 2 mm (0.079 in) and represents a typical value found in other experimental studies and reviews.[53,54,57,58] Note that similarly to hailstones, V_{wind} is augmented by a gust representing an increment in wind intensity due to the rain storm (see Eqn.24).

2. *Raindrop Damage*

Upon impact with a solid surface, a droplet is subject to a complex system of shock waves which lead to compressible behavior.[47,59,60] The instantaneous pressure P generated by the impact of a water raindrop with the blade solid surface may be evaluated through the modified water hammer pressure,[17,47,58,59,61–63] that is

$$P = \frac{Z_R\ V_{imp}\ \sin\theta}{1 + (Z_R/Z_C)} \tag{32}$$

where Z are the impedances for raindrop (R), and coating (C). By introducing also the impedance for the substrate (SS), the expressions for Z are

$$Z_R = \rho_R\ C_R; \qquad Z_C = \rho_C\ C_C; \qquad Z_{SS} = \rho_{SS}\ C_{SS} \tag{33}$$

Note that Z_{SS} is composed by a matrix and a fiber phase, depending on the fiber content of the material. The physical constants for raindrop, coating, and substrate are reported in Table 4. Once the droplet impact velocity V_{imp} and impact angle θ are known, the computation of the instantaneous pressures developed upon impact is complete. However, due to the largely subsonic impact speeds, it is likely that a single impact of a raindrop would not promote damage in the blade coating or substrate. For such reasons, it would be of particular interest being able to estimate the damage due to multiple raindrop impacts. In fact, the blade coating may weaken and be removed over time due to a fatigue mechanism imposed by numerous impacts on the same target.[15] The repetitive raindrop striking results in an erosion of the blade coating.

The approach implemented in the current study makes use of the damage model developed by Springer for coated composite materials subject to liquid droplet impact.[57] The advantage of doing so is in the ability to estimate the blade coating erosion rate, given the average stress on the coating surface. The erosion rate is a physical property associated with wear, and it is defined as the ratio of removed target material with respect to the unit mass of erodent.[64] In order to find an expression for the erosion rate, the average stress on the coating surface $\overline{\sigma_C}$ is derived from the modified waterhammer pressure, that is

$$\overline{\sigma_C} = P\ \frac{1+\psi_{SC}}{1-\psi_{SC}\ \psi_{RC}}\ \left[1 - \psi_{SC}\ \frac{1+\psi_{RC}}{1+\psi_{SC}}\ \frac{1-e^{-\gamma}}{\gamma}\right] \tag{34}$$

where the impedance ratios ψ are computed as

$$\psi_{SC} = \frac{Z_{SS} - Z_C}{Z_{SS} + Z_C}; \qquad \psi_{RC} = \frac{Z_R - Z_C}{Z_R + Z_C} \tag{35}$$

Table 5. Raindrop computational parameters

r/R	Re	AK_R	d_R/c	$V^0_{x,R}/V_r$	$V^0_{y,R}/V_r$	V_{rel}/V_r	We
0.35	5870	0.695	6.39×10^{-4}	1.239	0.099	1.243	60.7
0.70	10030	1.142	1.05×10^{-3}	1.115	0.074	1.117	177.1
0.90	12484	1.810	1.66×10^{-3}	1.087	0.061	1.089	274.4

while the expression for γ is given in the following form

$$\gamma = \frac{C_C}{C_R}\,\frac{d_R}{\delta_C}\,\frac{1+(Z_R/Z_{SS})}{1+(Z_C/Z_{SS})}\,\frac{2}{1+(Z_R/Z_C)} \tag{36}$$

Springer developed an empirical formula to express the erosion rate of a coating layer on top of a composite substrate as a function of $\overline{\sigma_C}$, the material impedances Z, and other structural parameters of the coating and of the composite substrate. The expression for the coating erosion rate E due to multiple raindrop impacts is written as

$$E = 0.023\,\left(\frac{1}{n_{i,C}}\right)^{0.7} \tag{37}$$

where $n_{i,C}$ represents the number of impacts per site during the incubation period on the coating. It is expressed as

$$n_{i,C} = 7\times10^{-6}\,\left(\frac{S_{eff,C}}{\overline{\sigma_C}}\right)^{5.7} \tag{38}$$

while the effective coating strength $S_{eff,C}$ is computed as

$$S_{eff,C} = \frac{4\;\sigma_{u,C}\,(b_C-1)}{(1-2\nu_C)\left(1+2\bar{k}\;\mid\psi_{SC}\mid\right)} \tag{39}$$

where $\sigma_{u,C}$ is the coating ultimate tensile strength and b_C is a dimensionless constant related to the coating fatigue curve. Finally, the expression for $\bar{k}$ is the following

$$\bar{k} = \frac{1-e^{-\gamma}}{1-\psi_{SC}\;\psi_{RC}} \tag{40}$$

Note that once the erodent, coating, and substrate materials are chosen, the values of Z, ψ, γ, $\bar{k}$, and $S_{eff,C}$ are constants and are evaluated only once at the beginning of the computations.

Similar to hailstones, an additional way to characterize the damage due to raindrops is by computing the impact force F_{imp} on the blade surface. A proposed form to estimate F_{imp} is given by the formula[47,48]

$$F_{imp} = m_R\,\frac{(V_{imp}\;\sin\theta)^2}{d_R} \tag{41}$$

Such a formula represents the average impact force due to a liquid droplet on a solid, motionless target.

The computational parameters and initial conditions for raindrops are summarized in Table 5, where the initial velocity components ($V^0_{x,R}$ and $V^0_{y,R}$), and the relative droplet velocity (V_{rel}) are nondimensionalized with respect to V_r.

IV. Results and Discussion

All simulations were performed by initializing BugFoil with the input parameters for hailstone and raindrop reported in Tables 3 and 5, respectively. Each location along the blade span was analyzed at three operating points corresponding to three angles of attack, as reported in Table 2. A single simulation required an average of 2 sec of computation time on an Intel Core i7 machine with 8 GB RAM running LinuxMint OS.

In order to characterize the particle impact locations along the airfoil, an appropriate figure of merit is the particle collection efficiency β, over the airfoil arc length s. The parameter s is defined as the length of the arc starting at the particle impact location and ending at the airfoil leading edge, normalized by the airfoil chord c. Note that s is negative for impingement locations on the lower side of the airfoil, while it is positive on the upper side. Also, the leading edge of a finite-thickness airfoil is located at $s\equiv0$, while the trailing edge corresponds to values of $|s|\geq1$. Results for impact of hailstone and raindrop are discussed in Sections B and C respectively.

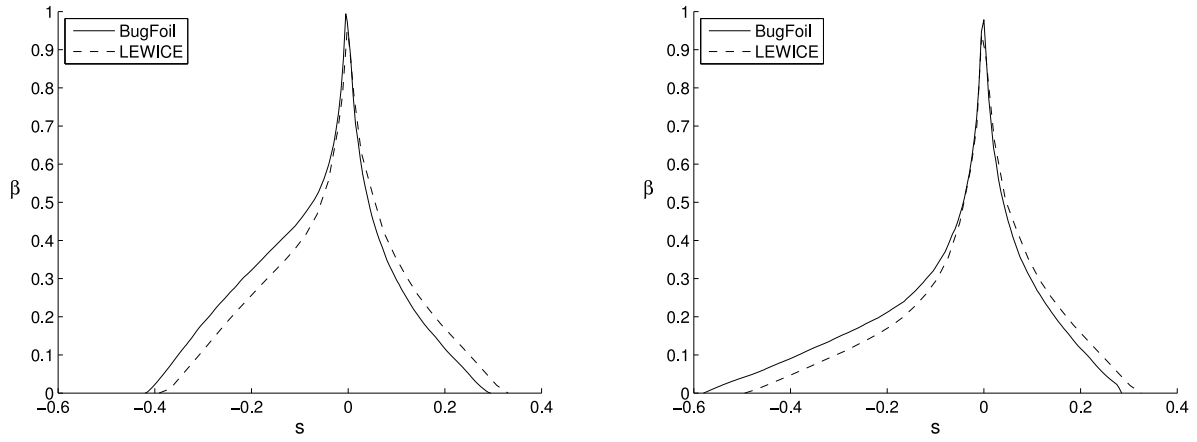

Figure 3. Comparison of BugFoil and LEWICE: β curves for rain at (a) r/R = 0.70, and (b) 0.90.

A. Code Validation

In order to evaluate the performance of BugFoil, it was performed a validation against the well-established droplet-icing code LEWICE.[65–67] LEWICE was used as a comparison of the water droplet trajectory against two airfoils at two different blade locations. In particular, it was chosen a rain drop diameter $d = 2$ mm, $\alpha = 6$ deg, and the blade locations at $r/R = 0.70$ and 0.90. The input conditions for the particles were identical to the conditions used for the blade analysis, and shown in Table 5. Note that LEWICE does not allow for a vertical component of the droplet velocity, and therefore both codes were initialized by neglecting such component.

Due to the different capabilities of the two codes, it was apparent to use the collection efficiency β as a benchmark. Figure 3 shows the comparison between the two codes for $r/R = 0.70$ [Fig. 3(a)], and $r/R = 0.90$ [Fig. 3(b)]. As it can be seen, BugFoil can predict closely the location and shape of the peaks at both bladespan locations. In particular, β has an excellent agreement in the region of $s = \pm 0.1$, where the largest damage on the blade is observed. However, the impingement limits appear to be consistently shifted toward smaller values of s at both bladespan locations. Moreover, during the validation procedure it was observed that a variation in angle of attack $\Delta\alpha \approx 2$ deg would allow for the tails of the β-curves to overlap. In particular, BugFoil displays very similar β curves for a reduced angle of attack, when compared with LEWICE. Such consideration suggested a substantial difference in the computed circulation around the airfoil, driven by differences in local pressure. However, as it can be noticed in Fig. 4, the coefficient of pressure C_P appears similar for both codes, and it rules out the hypothesis of differences in circulation.

Multiple tests of BugFoil were run using various resolutions for the impinging particles. Because LEWICE does not allow the user to fix the vertical spacing between particles upstream the airfoil, such parameter was varied in BugFoil to match the number of striking occurrences. However, even when this was accomplished, the shift in β curve was still present. Finally, the code was tested by perturbing the initial droplet input parameters, such as rain drop mass and diameter, but no appreciable convergence of the curves was observed.

By reading the manual for LEWICE,[65] it was found that the two codes handle the particle equations of motion differently. In particular, LEWICE makes use of the particle lift and gravitational force, whereas BugFoil neglects both. Unfortunately, a thorough treatment of the particle lift is not given in the manual, hence it was concluded that the two codes may have substantial differences in predicting the particle position, which drive the observed differences in β curves.

B. Hail Simulation

Hailstone trajectory is evaluated at the three locations along the blade span. Impingement efficiency β and damage velocity V_{dam} are plotted versus airfoil arc length s in Figs. 5, and 6. The β-curves of hailstones appear to reach a maximum at s = 0 for all three locations, as shown in Figs. 5(a), 5(b) and 5(c). Moreover, the maximum of β appears

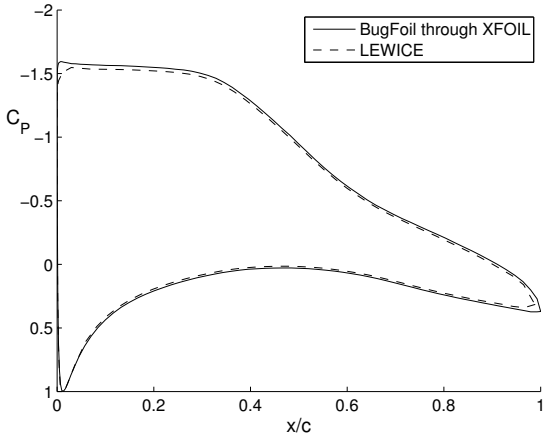

Figure 4. Comparison of codes – BugFoil vs. LEWICE; pressure coefficient C_P on a DU 96-W-180 airfoil, $\alpha = 6$ deg.

to be insensitive in amplitude and location with respect to angle of attack α. In fact, $\beta = 1$ is observed at all blade sections and for all considered angles of attack. The small sensitivity of the hailstones to the aerodynamic flowfield generated by the wind turbine blade is apparent. Because the hailstone mass is several orders of magnitude larger than particles such as sand grains, the observed behavior is physical. As a further proof of aerodynamic insensitivity, a fairly symmetrical shape of the β curve about $s = 0$ can be observed. The effect of the blade flowfield on both the blade suction and pressure sides has a limited effect on the impact s-location of hailstones.

Damage velocity V_{dam} along the blade is plotted in Fig. 6. The hailstone impact velocity reaches and exceedes the failure threshold velocity FTV at $r/R = 0.90$, promoting panel damage [Figs. 6(b) and 6(c)]. Peak values of V_{dam} are reached in the near proximity of $s = 0$ at that blade section, with a narrow range of s-values. Even though no damage was detected at $r/R = 0.35$ [Fig. 6(a)] and 0.70 [Fig. 6(b)], it should be noticed that a higher resolution of blade sections along the span would determine accurately the earliest panel delamination when moving toward the balde tip. The absence of damage for inboard sections is explainable when considering the local blade rotational velocity, which decrease linearly moving toward the blade hub.

Variations in angle of attack have little or no effect on V_{dam} at all three blade locations (Fig. 6), and such phenomenon follows the rationale previously explained about the hailstone β-curve sensitivity to α. In general, a narrow range of damaged panel surface is observed. This result is due to the FTE trigonometric function dependency on θ, shown in Eq. 26. Steeper impact angles occur at the blade leading edge, which corresponds to lower values of FTE. When moving downstream of the leading edge, θ decreases, causing FTE to increase, and therefore making it more difficult for hailstones to cause damage in the panel.

Impact efficiency E_I and damage ratio η_D versus α are plotted in Fig. 7. Values of E_I are consistently near unity for all blade sections and angles of attack, as shown in Fig. 7(a). This result is caused by the insensitivity of hailstones to aerodynamic perturbations due to the blade flowfield. In other words, hailstones impinge at nearly every location that the blade section shows along the particle path. However, by observing Fig. 7(b) a small portion of the impacting hailstones appear to promote delamination. In fact, η_D is greater than zero only for $r/R = 0.90$ where the impact velocity is high. Results show also that a variation in angle of attack reduces linearly the fraction of damaging hailstones when moving toward the blade tip. All the results are presented in Table 6 in terms of average and standard deviation of E_I and η_D.

The contours of damage velocity V_{dam} are plotted over the blade sections in Fig. 8. It can be observed that the extent of surface subject to hailstone impact is fairly large [Figs. 8(a), 8(b), and 8(a)]. However, FTV is reached only on a small region of the blade surface at $r/R = 0.90$, where the relative speed is high. Moreover, the whole lower side of the blade is exposed to hailstone impact at $\alpha = 6$ deg, even if the impact velocity is modest.

The hailstone impact force F_{imp} contours are shown in Fig. 9 for the three blade sections. At the inboard section ($r/R = 0.35$) [Fig. 9(a)] F_{imp} is modest, but it increases rapidly moving toward the blade tip [Figs. 9(b) and 9(c)]. In particular, F_{imp} can be approximated as $\propto V_r^2$. By analyzing Fig. 9 it can be seen that the highest impact forces occur at the very leading edge of the blade and the whole bottom surface is invested by hailstones, with modest values of

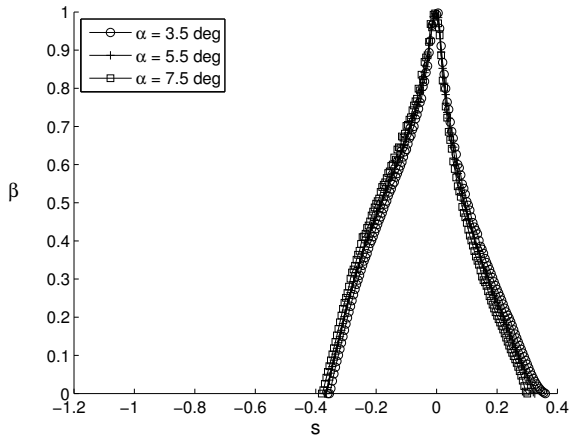

(a)

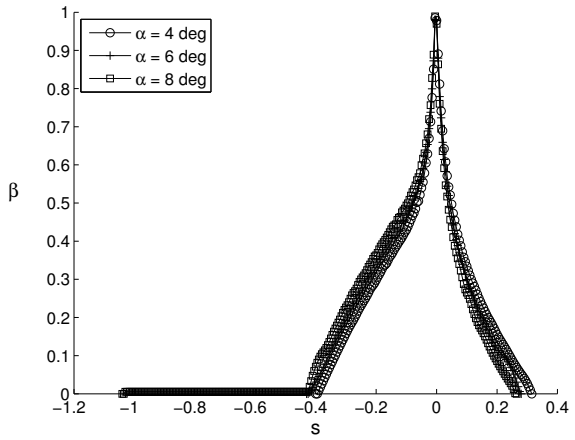

(b)

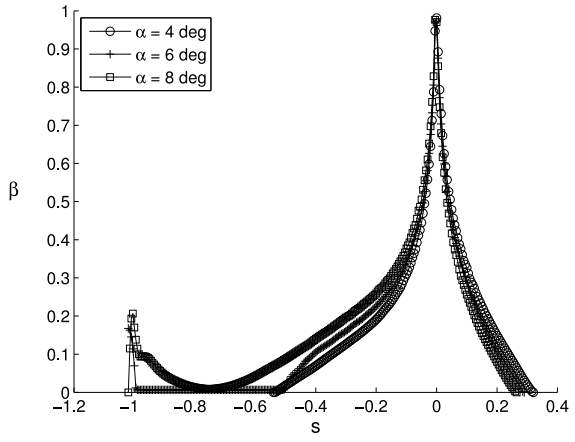

(c)

Figure 5. β curves for hail at (a) r/R = 0.35, (b) 0.70, and (c) 0.90.

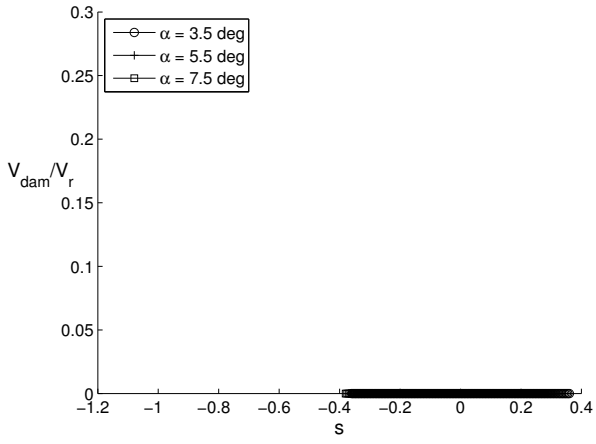

(a)

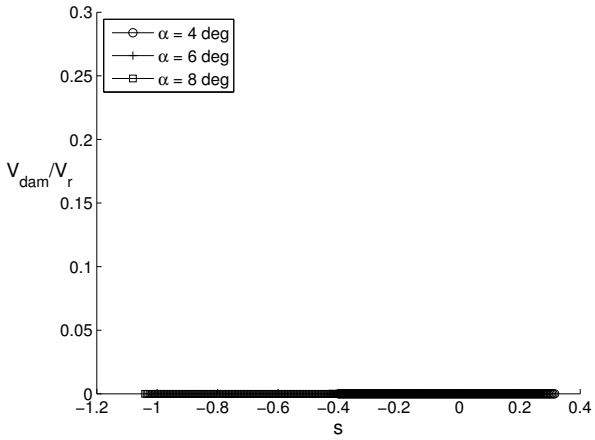

(b)

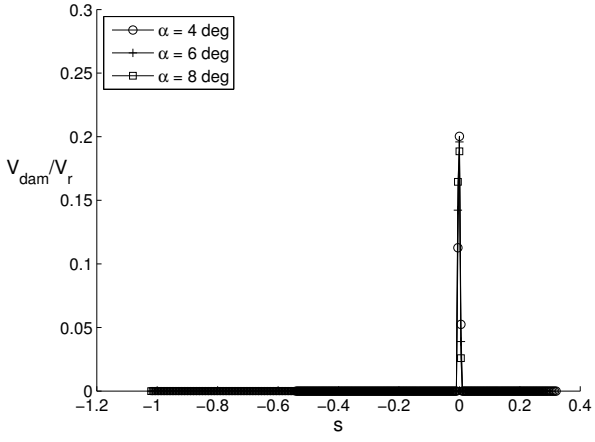

(c)

Figure 6. V_{dam} curves for hail at r/R = 0.35, (b) 0.70, and (c) 0.90.

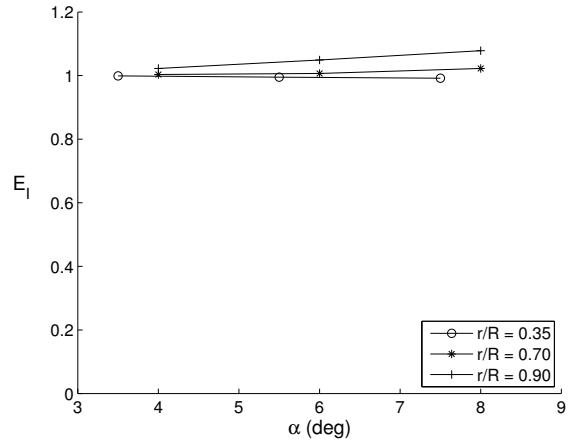

(a)

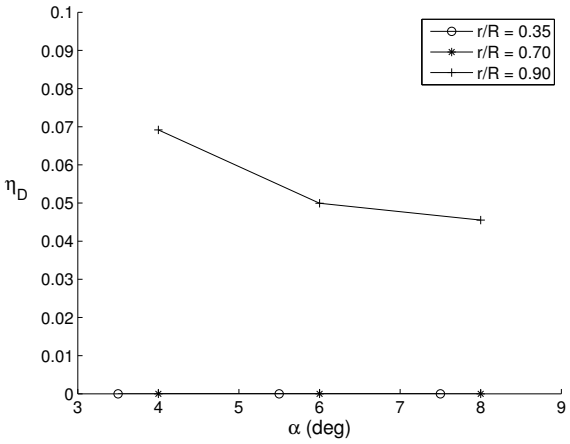

(b)

Figure 7. (a) Hail impingement efficiency E_I and (b) damage ratio η_D along the blade.

F_{imp} at the trailing edge. However, it is well known that blades are fairly weak with respect to strong impacts on the trailing edge, hence a valuable information comes from the present analysis.

C. Rain Simulation

The trajectory of falling raindrops is considered in this section. The curves of impingement efficiency β and erosion rate E are plotted versus airfoil arc length s in Figs. 10, and 11. Similarly to the hailstone case [see Fig. 5], the β-curves of raindrops have a maximum at $s = 0$ for all three locations, as shown in Figs. 10(a), 10(b) and 10(c). However, as opposed to the hailstone case, the maximum value of β never reaches the value of unity. Also, the peak of β is somewhat sensitive to variations in angle of attack α. In fact, for increasing α, the β-peak decreases in magnitude and moves toward the blade lower side ($s < 0$), following the stagnation point movement. By examining the upper impingement limits of raindrops, one can observe a consistent shift toward the blade leading edge for large values of α [Figs. 10(a), 10(b) and 10(c)]. The emerging information from this analysis is that the impingement pattern of raindrops is strongly correlated to the blade angle of attack and flowfield, as opposed to hailstones.

The erosion rate E of the coating for three blade sections is plotted in Fig. 11. The most apparent result of the computations is that E increases rapidly when moving from the blade inboard sections [Fig. 11(a)] toward more outboard sections [Figs. 11(b) and 11(c)]. Moreover, E is appreciable only on a small portion of the blade within the

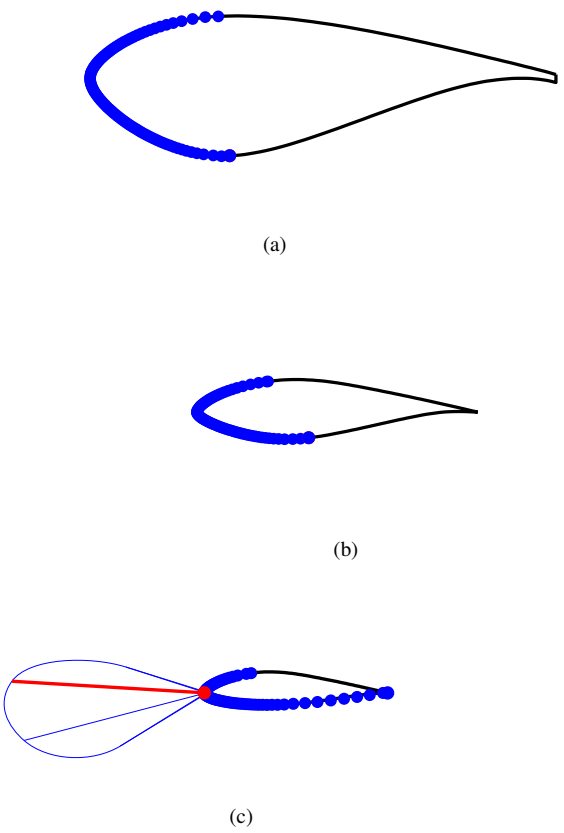

Figure 8. Contours of hailstone damage velocity V_{dam} at (a) r/R = 0.35 (α = 5.5 deg), (b) 0.70 (α = 6 deg), (c) and 0.90 (α = 6 deg); circles placed at impingement locations and red segments at maximum V_{dam}.

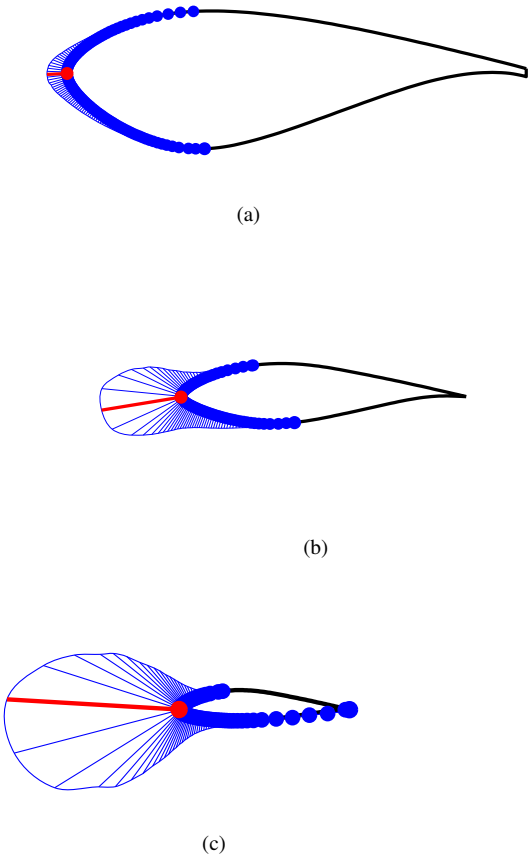

Figure 9. Contours of hailstone impact force F_{imp} at (a) r/R = 0.35 (α = 5.5 deg), (b) 0.70 (α = 6 deg), (c) and 0.90 (α = 6 deg); circles placed at impingement locations and red segments at maximum F_{imp}.

impingement limits. In fact, negligible values of E appear on the majority of blade surface subject to impingement, while most of the erosion is concentrated in the vicinity of the leading edge. Also, the shape of the E-curves suggests that the geometry of the leading edge modifies the pattern of the E-peaks. Blade sections with smaller leading edge radii have sharper peaks of E [Figs. 11(b) and 11(c)], compared with more inboard sections [Fig. 11(a)]. Finally, the effect of an increased α has a sensitive influence on the maximum value of E. In particular, at $r/R = 0.90$ [Fig. 11(c)] the erosion rate is about one third smaller when α is increased from 4 deg to 8 deg.

Rain impact efficiency E_I and impact surface ratio R_I are plotted versus α in Fig. 12. The most striking information obtained from E_I [Fig. 12(a)] is that large blade sections promote a more consistent deviation of rain drops, which is reflected by values of E_I smaller than unity at $r/R = 0.35$ and 0.70. In fact, thick blade sections perturb the flow early, allowing for rain drops to deviate from their path sooner. This observation is a further confirmation of the susceptibility of rain drops to the flowfield, through the local blade chord length and thickness. However, the blade angle of attack does not have a significant effect on E_I.

By examining Fig. 12(b) a mixed behavior of R_I can be observed with respect to α. In particular, the surface of the blade section that is mostly invested by rain drops is located at $r/R = 0.90$, and in general such value decreases when moving toward the hub. It can be concluded that at $r/R = 0.9$, the airfoil has the slimmest leading edge of those analyzed, allowing for larger surface areas exposed to rain impingement. On the contrary when moving inboard, the large leading edge radius shades the downstream parts of the blade, allowing for smaller values of R_I.

The contours of erosion rate E due to raindrops are displayed over the three blade sections in Fig. 13. First, a strong increase in E is evident when moving toward the blade tip. Also, the contours show that the extent of impinged

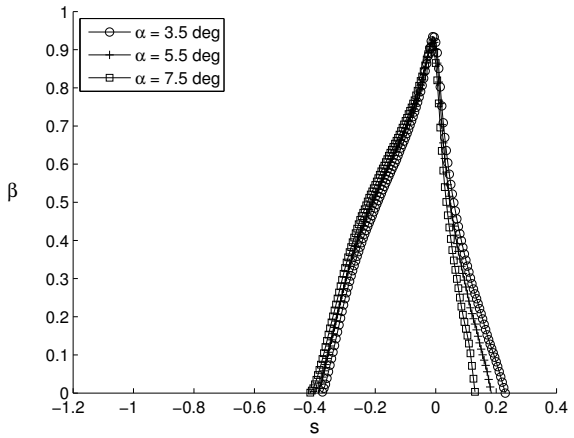

(a)

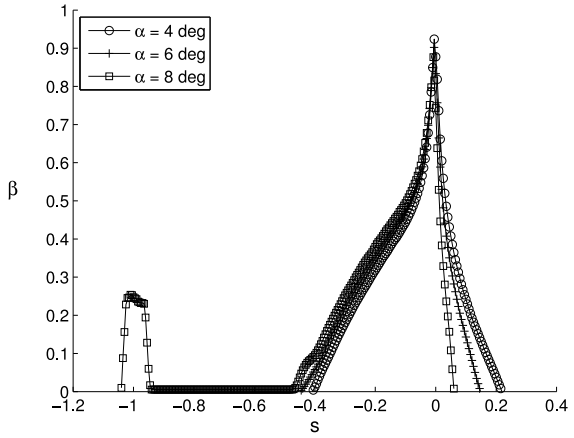

(b)

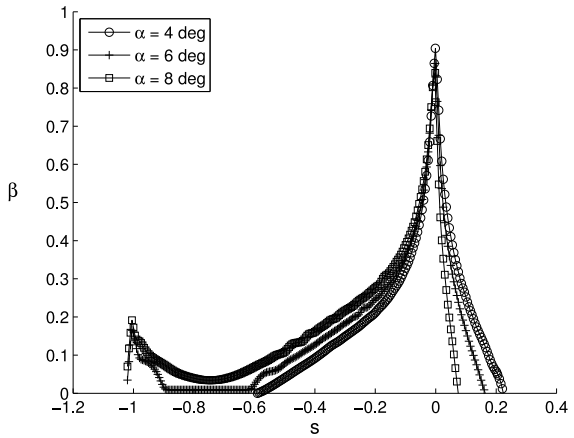

(c)

Figure 10. β curves for rain at (a) r/R = 0.35, (b) 0.70, and (c) 0.90.

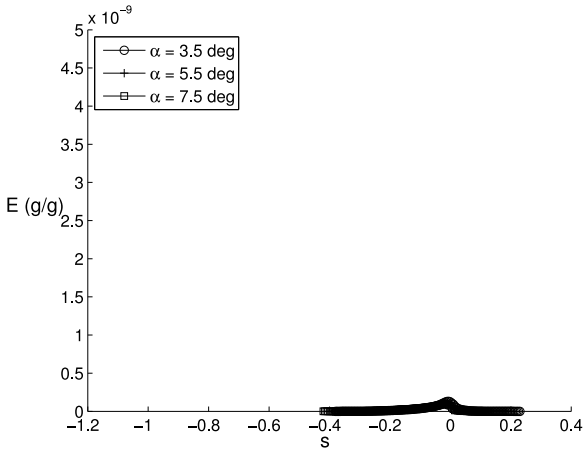

(a)

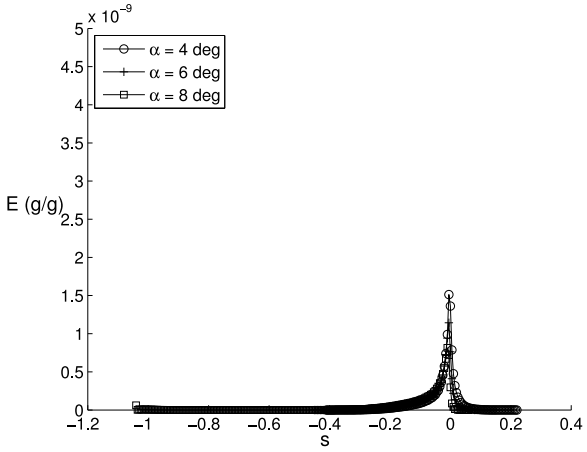

(b)

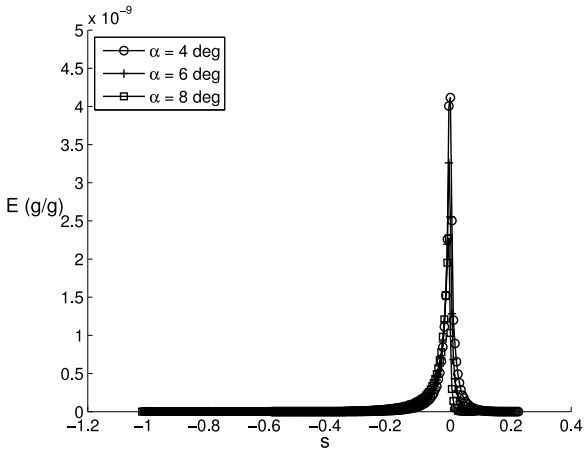

(c)

Figure 11. E curves for rain at (a) r/R = 0.35, (b) 0.70, and (c) 0.90.

Table 6. Average Values and Standard Deviations of Hail Impact Efficiency and Damage Ratio

Particle	r/R	$(E_I)_{avg}$	σ_{E_I}	$(\eta_D)_{avg}$	σ_{η_D}
Hail	0.35	0.995	3.50×10^{-3}	0.0	0.0
	0.70	1.011	1.03×10^{-2}	0.0	0.0
	0.90	1.050	2.79×10^{-2}	0.015	3.2×10^{-3}

blade surface is greater for the lower side of the blade, compared with the upper side. An explanation of such behavior comes from the sensitivity of raindrops to the blade flowfield and the geometry of the blade. In fact, once the blade is set at a given angle of attack, the incoming droplet may approach the upper side only tangentially, while striking a larger portion of the blade lower side.

The contours of droplet impact force F_{imp} are shown in Fig. 14. Similarly to hailstones [Fig. 9], F_{imp} is modest when considering the inboard section ($r/R = 0.35$) [Fig. 14(a)]. However, when moving toward the blade tip [Figs. 14(b) and 14(c)], F_{imp} increases rapidly. It has to be noted that the largest blade portion subject to rain impact lies below the blade stagnation point. Such behavior was explained in the previous paragraph, regarding the erosion rate E. As a further support of this observation, the blade sections with the bulkier leading edge [Figs. 14(a) and 14(b)] show larger portions of blade lower surface exposed to rain, when compared to the section with thinner leading edge [Fig. 14(c)]. A quick estimate of the rain drop damage with respect to blade velocity is proposed. From the E-contours [Fig. 13] it appears that the erosion rate is related to the cube of the local blade velocity, whereas F_{imp} shows a square power correlation to it [Fig. 14].

Finally, a comparison of the rain drop impact force is proposed at $r/R = 0.90$ for three angles of attack, as shown in Fig. 15. For all angles of attack, values of $F_{imp} \approx 10$ N are reached. However, by looking closely an increase in α causes a drop in F_{imp}. In particular, the maximum F_{imp} recorded at $\alpha = 8$ deg is about $1/3$ smaller than the maximum F_{imp} observed for $\alpha = 4$ deg. An explanation of such behavior is due to shape deformations of the rain drop as it approaches the blade surface while varying Weber number We. In fact, close to the stagnation point, the high-pressure regions of the lower surface will cause a relative flow that deforms the rain drop, increasing the drag coefficient. In other words, rain drops that impinge on the blade lower side will be slowed down more than rain drops impinging on the upper side of the blade. Such behavior will cause a more prominent damage when small angles of attack are considered.

V. Conclusions

The present work described a model to assess damage for wind turbine blades due to water-based atmospheric particles. Two types of particles were considered, namely hailstones and raindrops. Trajectories of impinging particles were evaluated through a numerical code and the properties at impact were computed. For both hailstones and rain drops, higher values of impingement efficiency E_I were observed for thinner airfoils, meaning a larger amount of particles were captured by the blade section when compared to thicker airfoils. Such behavior is physical, since small blade sections perturb the flow less upstream than thick and wider blade sections.

The simulations of hailstones showed that few particles promoting panel delamination were observed by moving toward the blade hub. This is due to the reduced local blade velocity at such locations. In fact, the impact velocity promoted panel damage when moving toward outboard blade sections, for $r/R \geq 0.90$. Finally, the impact forces developed by hailstones show prominent values on the very leading edge the blade, due to the incoming trajectory with respect to the blade surface. An estimate of the impact forces with respect to the blade relative wind shows that $F_{imp} \propto V_r^2$.

Table 7. Average Values and Standard Deviations of Rain Impact Efficiency

Particle	r/R	$(E_I)_{avg}$	σ_{E_I}	$(R_I)_{avg}$	σ_{R_I}
Rain	0.35	0.861	0.022	0.265	0.014
	0.70	0.893	0.023	0.370	0.135
	0.90	0.988	0.046	0.500	0.094

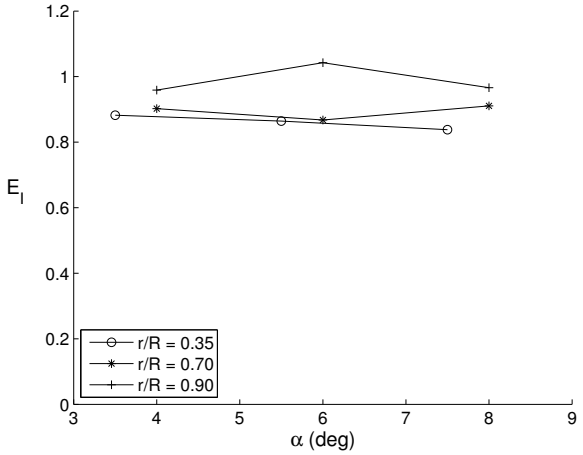

(a)

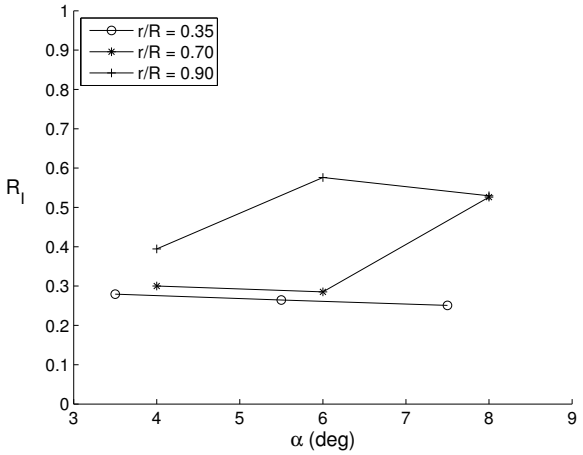

(b)

Figure 12. (a) Rain impingement efficiency E_I and (b) impact surface ratio R_I at three blade spanwise locations.

The analysis of rain drop impact showed that rain drops have a stronger sensitivity to the blade flowfield, when compared to hailstones. Such observation is reflected in the sensitivity of the impact force with respect to the blade angle of attack. It was also observed that the erosion rate due to rain drops follows the cubic power of the blade relative wind, whereas the impact force is related with a square power-law.

References

[1]Dalili, N., Edrisy, A., and Carriveau, R., "A Review of Surface Engineering Issues Critical to Wind Turbine Performance," *Renewable and Sustainable Energy Reviews*, Vol. 13, 2007, pp. 428–438.

[2]Sagol, E., Reggio, M., and Ilinca, A., "Issues Concerning Roughness on Wind Turbine Blades," *Renewable and Sustainable Energy Reviews*, Vol. 23, 2013, pp. 514–525.

[3]Ahmed, M. R., "Blade Sections for Wind Turbine and Tidal Current Turbine Applications – Current Status and Future Challenges," *International Journal of Energy Research*, Vol. 36, 2012, pp. 829–844.

[4]Hayman, B., Wedel-Heinen, J., and Brondsted, P., "Materials Challenges in Present and Future Wind Energy," *MRS Bulletin*, Vol. 33, April 2008, pp. 343–353.

[5]Singh, S., Bhatti, T. S., and Kothari, D. P., "A Review of Wind-Resource-Assessment Technology," Centre for Energy Studies, Indian Institute of Technology. Hauz Khas, New Delhi 110016, 2012.

[6]Ciang, C. C., Lee, J. R., and Bang, H. J., "Structural Health Monitoring for a Wind Turbine System: a Review of Damage Detection

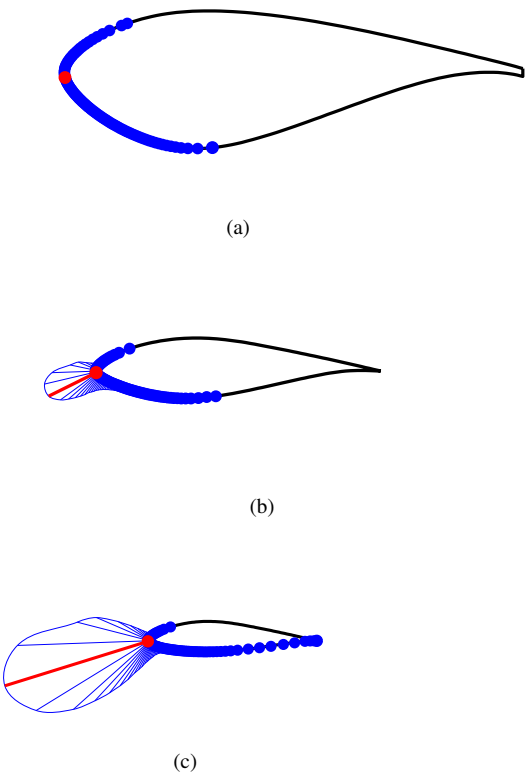

Figure 13. Contours of rain erosion rate E at (a) r/R = 0.35 (α = 5.5 deg), (b) 0.70 (α = 6 deg), (c) and 0.90 (α = 6 deg); circles placed at impingement locations and red segments at maximum E.

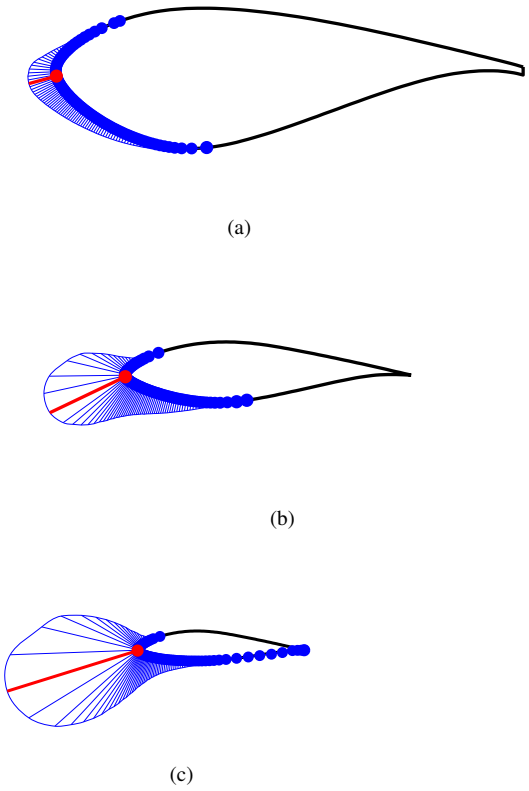

Figure 14. Contours of rain impact force F_{imp} at (a) r/R = 0.35 (α = 5.5 deg), (b) 0.70 (α = 6 deg), (c) and 0.90 (α = 6 deg); circles placed at impingement locations and red segments at maximum F_{imp}.

Methods," *Measurement Science and Technology*, Vol. 19, No. 12, Oct. 2008, pp. 122001–122021.

[7]Huang, C. W., Yang, K., Liu, Q., Zhang, L., Bai, J. Y., and Xu, J. Z., "A Study on Performance Influences of Airfoil Aerodynamic Parameters and Evalutation Indicators for the Roughness Sensitivity on Wind Turbine Blade," *Science China - Technological Sciences*, Vol. 54, No. 11, 2011, pp. 2993–2998.

[8]Mayor, G. S., Moreira, A. B. B., and Munoz, H. C., "Influence of Roughness in Protective Strips of Leading Edge for Generating Wind Profiles," *22nd International Congress of Mechanical Engineering*, COBEM 2013, 2013.

[9]Soltani, M. R., Birjandi, A. H., and Seddighi-Moorani, M., "Effect of Surface Contamination on the Performance of a Section of a Wind Turbine Blade," *Scientia Iranica B*, Vol. 18, No. 3, 2011, pp. 349–357.

[10]Ren, N. and Ou, J., "Dust Effect on the Performance of Wind Turbine Airfoils," *Journal of Electromagnetic Analysis and Applications*, Vol. 1, No. 2, 2009, pp. 102–107.

[11]Sareen, A., Sapre, C. A., and Selig, M. S., "Effects of Leading-Edge Protection Tape on Wind Turbine Blade Performance," *Wind Engineering*, Vol. 36, No. 5, 2012, pp. 525–534.

[12]van Rooij, R. P. J. O. M. and W.A.Timmer, "Roughness Sensitivity Considerations for Thick Rotor Blade Airfoils," *Proceedings of the 41st Aerospace Sciences Meeting and Exhibit*, AIAA Paper 2003-350, 2003.

[13]Arrighetti, C., Pratti, G. D., and Ruscitti, R., "Performance Decay Analysis of New Rotor Blade Profiles for Wind Turbines Operating in Offshore Environments," *Wind Engineering*, Vol. 27, No. 5, 2003, pp. 371–380.

[14]Kensche, C. W., "Fatigue of Composites for Wind Turbines," *International Journal of Fatigue*, Vol. 28, 2006, pp. 1363–1374.

[15]McGechaen, R. and Stack, M. M., "A Study of Raindrop Erosion of Steel and Polymer Based Composites: Application to Wind Turbines," Department of Mechanical Engineering, University of Strathclyde, James Weir Building, 75 Montrose St., Glasgow, G1 1XJ, Oct 2013.

[16]Zahavi, J. and Nadiv, S., "Indirect Damage in Composite Materials Due to Raidrop Impact," *Wear*, Vol. 72, 1981, pp. 305–313.

[17]Keegan, M. H., Nash, D. H., and Stack, M. M., "On Erosion Issues Associated with the Leading Edge of Wind Turbine Blades," *Journal of Physics D: Applied Physics*, Vol. 46, 2013, pp. 1–20.

[18]Ragheb, M., "USA Wind Energy Resources," University of Illinois at Urbana-Champaign, NPRE 475 lecture notes, Urbana, IL 61801, Jan 2010.

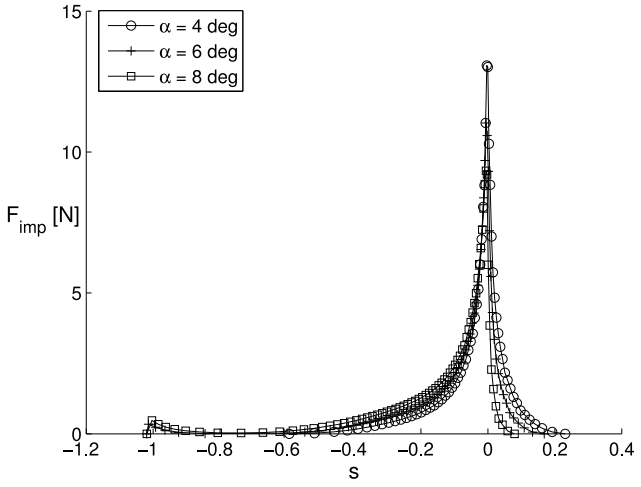

Figure 15. Comparison of rain instantaneous impact force F_{imp} at $r/R = 0.90$ for three angles of attack.

[19]Changnon, S. A., "Data and Approaches for Determining Hail Risk in the Contiguous United States," *Journal of Applied Meteorology*, Vol. 38, 1999, pp. 1730–1739.

[20]Edwards, R. and Hodanish, S. J., "Photographic Documentation and Environmental Analysis of an Intense, Anticyclonic Supercell on the Colorado Plains," *Monthly Weather Review - Picture of the Month*, Vol. 135, 2006, pp. 3753–3763.

[21]Tangler, J. L., "The Evolution of Rotor and Blade Design," *Presented at the American Wind Energy Association, Wind Power 2000*, NREL CP-500-28410, 2000.

[22]Hayman, B., "Approaches to Damage Assessment and Damage Tolerance for FRP Sandwich Structures," *Journal of Sandwich Structures and Materials*, Vol. 9, 2007, pp. 571–596.

[23]Kim, H. and Kedward, K. T., "Modeling Hail Ice Impacts and Predicting Impact Damage Initiation in Composite Structures," *AIAA*, Vol. 38, 2000, pp. 1278–1288.

[24]Rempel, L., "Rotor Blade Leading Edge Erosion - Real Life Experiences", Oct 2012, URL `http://www.windsytemsmag.com`.

[25]Ragheb, A. M. and Ragheb, M., "Wind Turbine Gearbox Technologies," *Fundamental and Advanced Topics in Wind Power*, edited by R. Carriveau, InTech, 2011, pp. 189–206.

[26]Hsu, D. K., Barnard, D. J., and Dayal, V., "NDE of Damage in Aircraft Flight Control Surfaces," *AIP Conference Proceedings, Review of Quantitative Nondestructive Evaluation*, American Institute of Physics 978-0-7354-0399, Apr 2007, 2007.

[27]Kim, H. and Funai, S., "Glancing Hail Impact on Composite Structures," Dept. of Structural Engineering, University of California at San Diego, La Jolla, CA 92093, Jun 2012.

[28]Thomsen, O. T., "Sandwich Materials for Wind Turbine Blades - Present and Future," *Journal of Sandwich Structures and Materials*, Vol. 11, No. 7, 2009, pp. 7–26.

[29]Kim, H., Welch, D. A., and Kedward, K. T., "Experimental Investigation of High Velocity Ice Impacts on Woven Carbon/epoxy Composite Panels," *Composites*, Vol. 34, 2003, pp. 25–41.

[30]Fiore, G. and Selig, M. S., "A Simulation of Operational Damage for Wind Turbines," *Proceedings of the 32nd AIAA Applied Aerodynamics Conference*, AIAA Paper 2014, 2014.

[31]Bragg, M. B. and Maresh, J. L., "A Numerical Method To Predict The Effect of Insect Contamination on Airfoil Drag," Aeronautical and Astronautical Engineering Report AARL 86-01, The Ohio State University Research Foundation, OH 43212, Mar 1986.

[32]Drela, M., "XFOIL: An Analysis and Design System for Low Reynolds Number Airfoils," *Low Reynolds Number Aerodynamics*, edited by T. J. Mueller, Vol. 54 of *Lecture Notes in Engineering*, Springer-Verlag, New York, June 1989, pp. 1–12.

[33]Roskam, J., *Airplane Flight Dynamics and Automatic Flight Controls*, DARcorp, Lawrence, KS 66044, 1995.

[34]Bragg, M. B., "Rime Ice Accretion and Its Effect on Airfoil Performance," NASA Lewis Research Center, NASA CR-165599, Mar 1982.

[35]Langmuir, I. and Blodgett, K., "Mathematical Investigation of Water Droplet Trajectories," Tech. Rept. 5418, U.S. Army Air Force, 1946.

[36]Tilly, G., "Erosion Caused by Airborne Particles," *Wear*, Vol. 14, No. 1, 1969, pp. 63–79.

[37]Hamed, A. A., Tabakoff, W., Rivir, R. B., Das, K., and Arora, P., "Turbine Blade Surface Deterioration by Erosion," *Journal of Turbomachinery*, Vol. 127, No. 3, 2005, pp. 445–452.

[38]Frost, W. and Aspliden, C., "Characteristics of The Wind," *Wind Turbine Technology, Fundamental Concepts of Wind Turbine Engineering, Second Edition*, edited by D. A. Spera, ASME Press, Three Park Avenue, New York City, NY 10016, 2009, pp. 467–541.

[39]Rhymer, J., Kim, H., and Roach, D., "The Damage Resistance of Quasi-Isotropic Carbon/Epoxy Composite Tape Laminates Impacted by High Velocity Ice," *Composites: Part A*, Vol. 43, 2012, pp. 1134–1144.

[40]Chang, F. K. and Qing, X. L., "Strength Determination of Mechanical Fastened Joints," *Recent Advances in Structural Joints and Repairs for Composite Materials*, edited by L. Tong and C. Soutis, Kluwer Academic Publishers, P.O. Box 17, 3300 AA Dordrecht, The Netherlands, 2003, pp. 101–140.

[41]Wilson, R. E., "Wind Turbine Aerodynamics Part A: Basic Principles," *Wind Turbine Technology, Fundamental Concepts of Wind Turbine Engineering, Second Edition*, edited by D. A. Spera, ASME Press, Three Park Avenue, New York City, NY 10016, 2009, pp. 281–350.

[42]Timmer, W. A. and van Rooij, R. P. J. O. M., "Summary of the Delft University Wind Turbine Dedicated Airfoils," *Journal of Solar Energy Engineering*, Vol. 125, No. 4, 2003, pp. 571–596.

[43]Zhou, Q., Li, N., Chien, X., Yonezu, A., Xu, T., Hui, S., and Zhang, D., "Water Drop Erosion on Turbine Blades: Numerical Framework and Applications," *Materials Transactions*, Vol. 49, 2008, pp. 1606–1615.

[44]DNV, "Design and Manufacture of Wind Turbine Blades, Offshore and Onshore Wind Turbines - October 2010," Standard DNV-DS-J102, Det Norske Veritas, Oct 2010.

[45]White, F. M., *Viscous Fluid Flow - Third Edition*, McGraw-Hill International Edition, New York, NY 10020, 2004.

[46]Hoerner, S. F., *Fluid-Dynamic Drag*, Hoerner Fluid Dynamics, Bakersfield, CA 93390, 1965.

[47]Field, J. E., "ELSI Conference: Invited Lecture, Liquid Impact: Theory, Experiment, Applications," *Wear*, Vol. 233, 1999.

[48]Nearing, M. A., Bradford, J. M., and Holtz, R. D., "Measurement of Force vs. Time Relations for Waterdrop Impact," *Soil Science Society of America Journal*, Vol. 50, No. 6, 1986, pp. 1532–1536.

[49]P. Van Der Leeden, L. D. N. and Suratman, P. C., "The Velocity of Free Falling Droplets," *Applied Science Research*, Vol. 5, 1955, pp. 338–348.

[50]Gunn, R. and Kinzer, G. D., "The Terminal Velocity of Fall for Water Droplets in Stagnant Air," Tech. rept., U.S. Weather Bureau, 1949.

[51]Foote, G. B. and du Toit, P. S., "Terminal Velocity of Raindrops Aloft," *Journal of Applied Meteorology*, Vol. 8, 1968, pp. 249–253.

[52]Pilch, M. and Erdman, C., "Use of Breakup Time Data and Velocity History Data to Predict the Maximum Size of Stable Fragments for Acceleration-Induced Breakup of a Liquid Drop," *International Journal Multiphase Flow*, Vol. 13, No. 6, 1987, pp. 741–757.

[53]Vargas, M. and Feo, A., "Experimental Observations on the Deformation and Breakup of Water Droplets Near the Leading Edge of an Airfoil," NASA Technical Memorandum, 2011-216946, NASA Glenn Research Center, Cleveland, OH, 44135, Jan 2011.

[54]Gohardani, O., "Impact of Erosion Testing Aspects on Current and Future Flight Conditions," *Progress in Aerospace Sciences*, Vol. 47, 2011, pp. 280–303.

[55]Vargas, M., Sor, S., and Magarino, A. G., "Drag Coefficient of Water Droplets Approaching the Leading Edge of an Airfoil," *Proceedings of the 5th Atmospheric and Space Environments Conference*, AIAA, 2013.

[56]Schmehl, R., "Advanced Modeling of Droplet Deformation and Breakup for CFD Analysis of Mixture Preparation," *ILASS-Europe*, 2002.

[57]Springer, G. S., *Erosion by Liquid Impact*, Scripta Technica, Inc., Washington, D.C., 1976.

[58]Keegan, K. H., Nash, D. H., and Stack, M. M., "Modelling Rain Drop Impact of Offshore Wind Turbine Blades," *Proceedings of the TURBO EXPO*, 2012.

[59]Field, J. E., "The Physics of Liquid Impact, Shock Wave Interactions With Cavities, and the Implications To Shock Wave Lithotripsy," *Physics in Medicine and Biology*, Vol. 36, No. 11, 1991, pp. 1475–1484.

[60]Obreschkow, D., Dorsaz, N., de Bosset, A., Tinguely, M., Field, J., and Farhat, M., "Confined Shocks Inside Isolated Liquid Volumes – A New Path of Erosion?" *Physics of Fluids*, Vol. 23, 2011.

[61]G. F. Schmitt Jr., "Liquid and Solid Particle Impact Erosion," AFML-TR 79-4122, Air Force Materials laboratory, 1979.

[62]Dear, J. P. and Field, J. E., "High-Speed Photography of Surface Geometry Effects in Liquid/Solid Impact," *Journal of Applied Physics*, Vol. 63, No. 4, 1988, pp. 1015–1021.

[63]Heymann, F., "High-Speed Impact Between a Liquid Drop and a Solid Surface," *Journal of Applied Physics*, Vol. 40, No. 13, 1969, pp. 5113–5122.

[64]Davis, J. R., editor, *Surface Engineering for Corrosion and Wear Resistance*, chap. 3, ASM International - The Materials Information Society, 10M Communications, Materials Park, OH 44073-0002, 2001, pp. 43–86.

[65]Wright, W., "User's Manual for LEWICE Version 3.2," NASA Glenn Research Center NASA/CR–2008-214255, QSS Group, Inc., Cleveland, Ohio 44135, Nov 2008.

[66]Fujiwara, G. E. C., Woodard, B., Wiberg, B., Mortonson, A., and Bragg, M., "A Hybrid Airfoil Design Method for Icing Wind Tunnel Tests," *Fluid Dynamics and Co-located Conferences, 5th AIAA Atmospheric and Space Environments Conference, American Institute of Aeronautics and Astronautics*, AIAA, 2013.

[67]Fujiwara, G. E. C., Wiberg, B., Woodard, B., and Bragg, M., "3D Swept Hybrid Wing Design Method for Icing Wind Tunnel Tests," *6th AIAA Atmospheric and Space Environments Conference, American Institute of Aeronautics and Astronautics,*, AIAA, 2014.